

Article

Polypyrrole Film Deposited-TiO₂ Nanorod Arrays for High Performance Ultraviolet Photodetectors

Huan Wang¹, Pei Qin^{2,3}, Yun-Hui Feng^{1,*}, Hui-Liang Sun¹, Hui-Xiang Wu¹, Bo-Kai Liao¹, Yue-Bin Xi⁴ and Wei Wang^{1,*}

¹ Guangzhou Key Laboratory of Sensing Materials & Devices, Center for Interdisciplinary Health Management Studies, School of Chemistry and Chemical Engineering, Guangzhou University, Guangzhou 510006, China; cewanghuan@gzhu.edu.cn (H.W.); huiliang@gzhu.edu.cn (H.-L.S.); cce.whx@gzhu.edu.cn (H.-X.W.); bokailiao@gzhu.edu.cn (B.-K.L.)

² School of Chemical Engineering and Light Industry, Guangdong University of Technology, Guangzhou 510006, China; qinpei@gz.iscas.ac.cn

³ Guangzhou Institute of Software Application Technology, No. 1121 Haibin Road, Nansha District, Guangzhou 511400, China

⁴ Key Laboratory of Pulp and Paper Science & Technology of Ministry of Education, State Key Laboratory of Biobased Material and Green Papermaking, Qilu University of Technology (Shandong Academy of Sciences), Jinan 250353, China; qlgdxyb@qlu.edu.cn

* Correspondence: alleypop@gzhu.edu.cn (Y.-H.F.); wangw@gzhu.edu.cn (W.W.)

Abstract: TiO₂-based ultraviolet photodetectors have drawn great attention and are intensively explored. However, the construction of TiO₂-based nanocomposites with excellent ultraviolet responses remains challenging. Herein, a TiO₂ nanorod array was successfully prepared on fluorine-doped tin oxide (FTO) conductive glass by a one-step hydrothermal method. Then, polypyrrole (PPy)-TiO₂ nanorod array composites were designed via subsequent in situ oxidative polymerization. The morphologies, structures, and photocurrent responses of the nanocomposites were systematically investigated. The results demonstrated that polypyrrole-TiO₂ exhibited a stronger photocurrent response than pure TiO₂ due to the p-n junction formed between n-type TiO₂ nanorod arrays and p-type polypyrrole. The PPy-TiO₂ composite obtained by deposition three times had the best photoelectric properties, exhibiting good performance with a sensitivity of 41.7 and responsivity of 3.5×10^{-3} A/W. Finally, the mechanism of the photoelectrical response of PPy-TiO₂ composites was discussed, guiding the design of high-performance TiO₂-based ultraviolet photodetectors.

Keywords: titanium oxide; ultraviolet photodetectors; polypyrrole; nanocomposites; p-n junction



Citation: Wang, H.; Qin, P.; Feng, Y.-H.; Sun, H.-L.; Wu, H.-X.; Liao, B.-K.; Xi, Y.-B.; Wang, W. Polypyrrole Film Deposited-TiO₂ Nanorod Arrays for High Performance Ultraviolet Photodetectors. *Chemosensors* **2022**, *10*, 277. <https://doi.org/10.3390/chemosensors10070277>

Academic Editor: Filippo Giubileo

Received: 6 June 2022

Accepted: 11 July 2022

Published: 13 July 2022

Publisher's Note: MDPI stays neutral with regard to jurisdictional claims in published maps and institutional affiliations.



Copyright: © 2022 by the authors. Licensee MDPI, Basel, Switzerland. This article is an open access article distributed under the terms and conditions of the Creative Commons Attribution (CC BY) license (<https://creativecommons.org/licenses/by/4.0/>).

1. Introduction

The basic working principle of ultraviolet (UV) photodetectors is that light is irradiated on photoresponsive material, which absorbs the energy of the photon and can excite photogenic electron-hole pairs thus showing the current signal, which can be applied to the detection of the light signal. UV photodetectors have gained intensive interest in the fields of industrial manufacture, biological detection, and environment monitoring due to the coupling merits of high sensitivity, good selectivity, and low cost [1–3]. The performance of UV photodetectors is closely related to the structure and properties of photosensitive materials. In recent years, diverse wide bandgap semiconductors such as SiC, GaN, ZnO, NiO, and TiO₂ have been widely applied in the fabrication of UV photodetectors [4–8]. Among them, TiO₂ has received widespread attention because of its tunable nanostructure, non-toxicity, and chemical stability [9–11]. However, the low mobility and high recombination rate of photogenerated carriers in TiO₂ greatly hinder its application performance in UV photodetectors.

The photoresponse performance, sensitivity, and stability of UV photodetectors can be significantly improved by constructing a semiconductor heterojunction. Bulk TiO₂ is a

typical n-type semiconductor material. The p-n heterojunction can be constructed using an in situ composite with a p-type conductive polymer to improve its photoelectric response. The Schottky heterojunction can be constructed using a recombination of metal nanoparticles to provide it with excellent photoelectric response performance. So far, tremendous efforts have been made to design high-performance TiO₂-based UV photodetectors by constructing p-n junctions, Schottky junctions, and heterojunctions for their fast photo-excited electron-hole pair separation [12–16]. Yang et al. [15] fabricated all-solid-state NiO/TiO₂ heterojunctions with the NiO layer above or below TiO₂ nanoarrays, and the fabricated devices demonstrated high detection sensitivity, fast photoresponse time, and self-powered performance. Wang et al. [16] assembled a UV sensor based on vertically aligned TiO₂ nanowire arrays interconnected with ZnO nanosheets, which achieved UV light sensing performance. In addition to metal oxides, conducting polymers with good conductivity and reversible chemical states have also been used to improve the UV response of TiO₂ [17–21]. Che et al. [20] fabricated TiO₂ nanoarrays/PEDOT-type conducting polymers composites via electrochemical polymerization, which achieved good UV photo-detection performances. Kareem et al. [21] synthesized a nanocomposite composed of polypyrrole (PPy) nanofibers and TiO₂ nanoparticles, which showed improved optical sensitivity. These results indicate that UV photodetectors with good performance can be obtained by constructing semiconductor composite materials, especially by constructing heterojunctions.

The formation of a heterojunction is closely related to the interface contact state of semiconductor composites. Therefore, high efficiency, large scale, and stable construction of nano-composites with controllable microstructure and morphology are the premise of preparing photoelectric devices with excellent performance by developing an appropriate preparation process. Good interface contact is the prerequisite for the formation of a stable heterojunction. The spin-coating method is simple and easy to operate, which can fabricate composite devices on a large scale, but the interface contact is difficult to control. Electrochemical in situ polymerization has the advantages of high efficiency, simplicity, and easy operation, but it has a narrow application range and can be applied to fewer systems. The interface contact formed by in situ chemical polymerization is close and stable, but the efficiency of this method is low. In our previous research, TiO₂/PANI nanocomposites with controllable microstructure were successfully prepared by in situ chemical polymerization and low-speed spin coating, which showed excellent photoelectric response performance. These works provide a solid foundation for further preparation of other TiO₂ composites and the study of their photoelectric response properties.

The above findings demonstrated that the interface contact between the conducting polymer and TiO₂ would greatly influence the optical properties of their nanocomposites. Therefore, it is highly desired to develop suitable approaches to tailor interface bonding of PPy-TiO₂-based nanocomposites for high-performance UV photodetectors. In this work, we first successfully prepared TiO₂ nanoarrays with regular microstructure through a simple hydrothermal method. Additionally, then PPy film-coated-TiO₂ nanorod arrays were successfully synthesized via in situ oxidative polymerization. The thickness of PPy film can be effectively controlled by the number of deposition times. The structural characteristics and the optical properties of the as-prepared PPy-TiO₂ nanocomposites were systematically investigated.

2. Materials and Methods

2.1. Chemical Reagents

Acetone (AR, 99.8%), anhydrous ethanol (AR, 99.5%), and hydrochloric acid (37 wt.%) were purchased from Guangzhou Chemical Reagent Factory (Guangdong, China). Titanium butoxide (AR, 98%) was purchased from Shanghai Macklin Biochemical Co., Ltd. (Shanghai, China), and pyrrole (Py, AR, 98%) and ammonium persulfate (APS, AR, 99%) were purchased from Shanghai Aladdin Biochemical Technology Co., Ltd. (Shanghai, China). All reagents were used directly without further treatment. Fluorine-doped tin oxide (FTO) substrates were purchased from Nippon Sheet Glass Co., Ltd. (Osaka, Japan).

2.2. Preparation of the TiO₂ Nanorod Arrays

TiO₂ nanorod arrays were synthesized via a simple hydrothermal method [22]. Fluorine-doped tin oxide (FTO) substrate (25 mm × 25 mm, Nippon Sheet Glass Co., Ltd.) was ultrasonically cleaned for 30 min in acetone, ethanol, and deionized water thrice and was placed into a Teflon-liner stainless steel autoclave. A mixed solution of 30 mL of deionized water, 30 mL of HCl (~37 wt%), and 1 mL of titanium butoxide was then poured into the autoclave. The autoclave was sealed and transferred to an oven at 150 °C for 20 h. After the autoclave cooled down to room temperature, the FTO substrate was taken out and rinsed with deionized water five times to obtain TiO₂ nanorod arrays grown on the FTO substrate.

2.3. Preparation of the PPy-TiO₂ Nanocomposites

PPy-TiO₂ nanocomposites were synthesized via in situ oxidative polymerization as follows: Firstly, 160 µL pyrrole were added to 20 mL of 1 M HCl and stirred for 1 min. Secondly, the prepared TiO₂ nanorod arrays were placed in the above solution, and 1.5 mL of 0.1 M APS solution were dropped into the solution. Subsequently, the mixed solution was placed into a refrigerator at 0 °C for 1 h to acquire PPy-TiO₂ nanocomposites. By controlling the reaction times, nPPy-TiO₂ nanocomposites obtained by different deposition times were prepared, where n represented the deposition times (n = 1, 2, 3, and 4).

2.4. Fabrication of the FTO-nPPy-TiO₂-FTO Device

The schematic diagram of the fabrication of the FTO-nPPy-TiO₂-FTO device is shown in Figure 1. A cleaned FTO substrate was taken, and its conductive surface was fixed face to face with the nPPy-TiO₂ nanocomposites on FTO to obtain the FTO-nPPy-TiO₂-FTO photodetectors. For comparison, the FTO-TiO₂-FTO device was fabricated using a cleaned FTO substrate and the FTO substrate that coated the TiO₂ nanorod arrays.

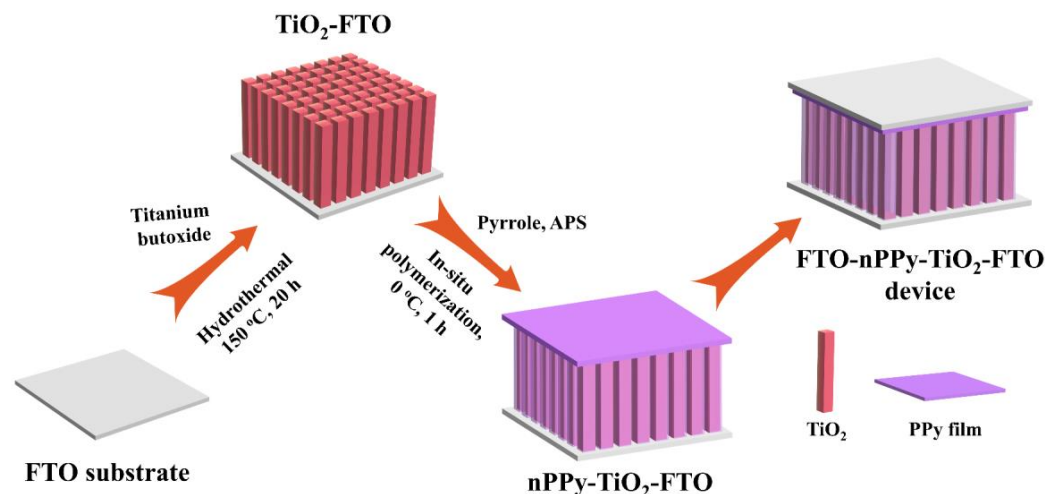


Figure 1. Schematic diagram of the fabrication of the FTO-nPPy-TiO₂-FTO device.

2.5. Characterization

The morphologies of the samples were observed by scanning electron microscopy (SEM, JEOL, JSM-7001F, Rigaku Tokyo, Japan) and transmission electron microscopy with energy-dispersive spectroscopy (TEM, FEI Talos F200X, Thermo Fisher Scientific, USA). For the TEM measurement, the PPy-TiO₂ composite was first scraped off the FTO substrate, then dispersed in anhydrous ethanol, and the supernatant was dropped onto a copper mesh after 1 h of sonication and air-dried for use. The structural characteristics of the samples were examined by Raman spectroscopy (LabRAM HR800, HORIBA Jobin Yvon, Japan). The crystalline structures of the samples were characterized by X-ray diffraction (XRD, Bruker D8 Advance, Germany). The surface properties of the samples were studied by X-ray photoelectron spectroscopy (XPS, Thermo Scientific K-Alpha, Thermo Fisher Scientific,

USA), where the charge correction was based on a binding energy of 284.8 eV for C1s. UV-Vis absorption spectra of the samples were recorded using a UV-Vis spectrophotometer (UV 2450, Shimadzu, Japan). Photoluminescence (PL) spectra were used to investigate the optical properties of the samples (FluoroMax-4, HORIBA Jobin Yvon, Japan). The photoelectric performances of the fabricated devices were measured by a CHI660D electrochemical workstation (Chenhua, Shanghai), where electrochemical impedance spectroscopy (EIS) was performed at the open-circuit voltage of the device; the test frequency ranged from 0.01 to 100,000 Hz, and the amplitude was set to 5 mV. The UV light source was provided by a portable UV lamp (~8W, ENF-280C, Spectronics, USA). The overall sensing area of the fabricated UV photodetector was about 1.5 cm². The UV light irradiated the device at an incident angle of 30°.

3. Results and Discussion

3.1. Structural and Optical Properties of the PPy-TiO₂ Nanocomposites

The cross-sectional morphologies of all the nPPy-TiO₂ nanocomposites prepared by different deposition times were first observed by SEM, as shown in Figure 2. Both samples showed similar morphologies, where PPy film was deposited on the surface of TiO₂ nanorods, and the thickness of the PPy layer can be effectively controlled from 20 nm~200 nm. With the increasing deposition times, the thickness of PPy film that coated the surface of TiO₂ nanorod arrays gradually increased, and the TiO₂ nanorod arrays remained neatly arranged. It can be seen that uniform PPy film was deposited on the TiO₂ nanorods in 3PPy-TiO₂ owing to the strong hydrogen bonding interaction between the hydroxyl groups on the TiO₂ surface and PPy, but with further deposition, aggregated PPy particles appeared in 4PPy-TiO₂ due to the completely covered binding sites on the TiO₂ surface, which indicated that the optimized deposition times were three times. The above results suggested that the morphologies of the PPy-TiO₂ composites can be precisely regulated by the number of PPy depositions. TEM measurement was further conducted to study the interfacial recombination between the PPy and TiO₂. The TEM images in Figure 3a,b further revealed the microstructure of 3PPy-TiO₂, where a well-defined composite interface labelled by yellow and white lines between the PPy and TiO₂ array could be observed, indicating the good compatibility of the composite. The TiO₂ array was composed of a large number of small nanorods with sizes of about 5 nm and lengths of about 1.1 μm (Figure S1), which is conducive to receiving more light stimulation and thus enhancing the photo response performance. The clear lattice fringes of the HRTEM image in Figure 3c demonstrated that the deposition of PPy would not destroy the lattice structure of titanium dioxide. The interlayer spacing of 0.223 nm in Figure 3c was assigned to the (200) crystal plane of rutile TiO₂, and the corresponding selected area electron diffraction pattern in Figure 3d show its typical single-crystal characteristics. Furthermore, the STEM image in Figure 3e and the elemental mapping images in Figure 3f-i show the uniform distribution of C, N, O, and Ti elements, suggesting uniform PPy deposition on TiO₂ nanorods. This might favor the good optical property of 3PPy-TiO₂.

Raman spectroscopy was conducted to examine the structural properties of pure TiO₂ and nPPy-TiO₂ nanocomposites. As illustrated in Figure 4a, pure TiO₂ showed three peaks at 228, 435, and 598 cm⁻¹ assigned to the characteristic signals of rutile TiO₂ [23,24]. After PPy deposition, these three peaks were slightly blue-shifted, indicating the existence of chemical bonding between PPy and TiO₂ nanorods. The chemical bonding may result from the hydrogen bonding between the amino group of PPy and the surface hydroxyl group of TiO₂, and the light scattering ability of TiO₂ was changed. Several new peaks attributed to PPy also appeared in the range of 800~1800 cm⁻¹. Namely, characteristic peaks at 930, 1050, 1080, and 1252 cm⁻¹ were the result of C-H deformation vibration in PPy [25,26], the double peak at 1374 and 1332 cm⁻¹ was the ring stretching vibration peak of pyrrole [27,28], and the single peak at 1595 cm⁻¹ was indexed to the C=C stretching vibration of pyrrole ring [29,30]. Furthermore, the characteristic peak intensity of TiO₂ in the nPPy-TiO₂ composites gradually weakened with the increased deposition times, indicating

that rutile TiO_2 had been completely covered by the newly generated PPy film. All XRD patterns in Figure 4b show diffraction peaks at $2\theta = 37.7^\circ, 39.4^\circ, 56.1^\circ, 64.4^\circ, 70.6^\circ,$ and 71.4° that can be indexed to (101), (200), (220), (310), (301), and (112) crystal planes of rutile TiO_2 (JCPDS No. 21-1276) [8], indicating the deposition of PPy did not change the crystal structure of TiO_2 . These results are consistent with the analysis of TEM. Noteworthy, the relative intensity of the diffraction peak of the (002) crystal plane in the PPy/ TiO_2 composite was weakened compared to pure TiO_2 , indicating that PPy was preferentially deposited on the (002) crystal plane of TiO_2 . XPS measurements were further conducted to detect the interface interaction between PPy and TiO_2 . Figure 4c show the XPS surveys of TiO_2 and 3PPy- TiO_2 , where a typical N1s signal assigned to PPy and a weakened Ti2p signal appeared, and the Sn3d signal inherited from the FTO substrate disappeared after PPy deposition, suggesting the successful combination of TiO_2 and PPy. It was noteworthy that the Ti2p_{1/2} and Ti2p_{3/2} of 3PPy- TiO_2 up-shifted by 0.2 eV concerning their positions in pure TiO_2 in Figure 4d, indicating the electron transfer from PPy to TiO_2 owing to the strengthened interface interaction [31,32], which was beneficial for the improvement of the photoelectric response of 3PPy- TiO_2 .

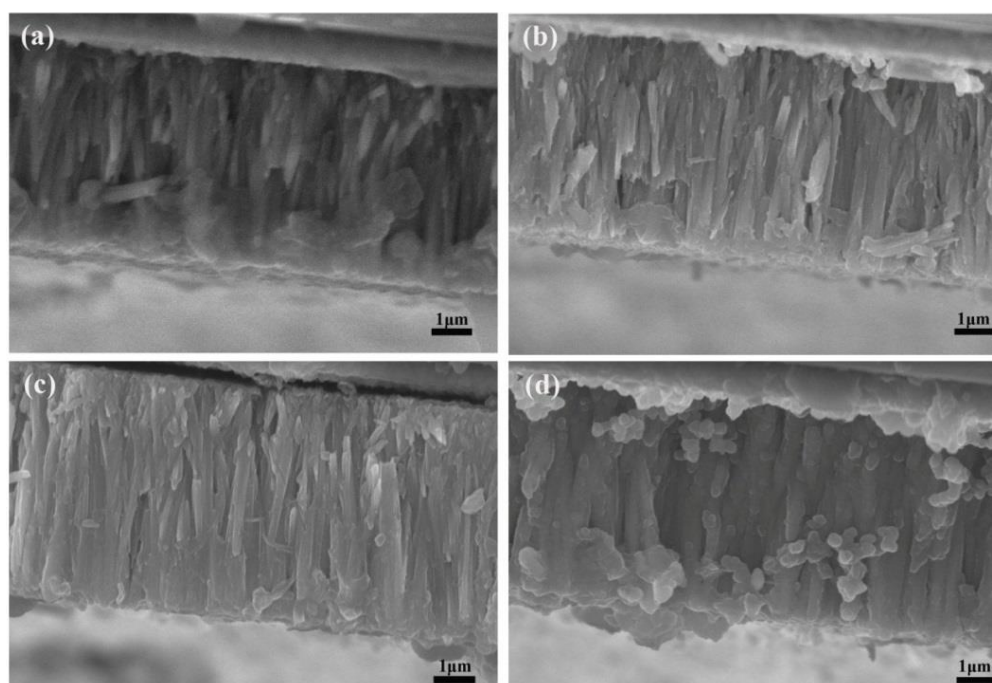


Figure 2. Cross-sectional SEM images of PPy- TiO_2 nanocomposites prepared by different deposition times, (a) 1PPy- TiO_2 , (b) 2PPy- TiO_2 , (c) 3PPy- TiO_2 , and (d) 4PPy- TiO_2 .

The optical properties of pure TiO_2 and nPPy- TiO_2 nanocomposites were then characterized by UV-Vis absorption spectra and a photoluminescence spectrum. As shown in Figure 5a, pure TiO_2 displayed an absorption edge around 420 nm, implying a band gap of 3.0 eV of rutile TiO_2 [33]. The absorption edges of nPPy- TiO_2 nanocomposites were around 410 nm, which suggested that PPy changed the band gap of the prepared TiO_2 . Both nPPy- TiO_2 nanocomposites exhibited stronger absorption than pure TiO_2 under UV light in the wavelength ranging from 220 to 400 nm, indicating PPy deposition could extend the optical response range of TiO_2 nanorod arrays. However, excessive deposition in 4PPy- TiO_2 caused a thick PPy film that blocked UV absorption, leading to decreased absorption compared to 3PPy- TiO_2 . Figure 5b plot the PL features of the pure TiO_2 and nPPy- TiO_2 nanocomposites, where the peak at 412 nm should stem from the band edge recombination process of TiO_2 [34], the peak at 450 nm might be attributed to inter-band recombination [35], and the signal at 467 nm should correspond to oxygen vacancies [36]. Meanwhile, both nPPy- TiO_2 nanocomposites showed lower PL intensity than pure TiO_2 ,

resulting from the strong visible light absorption and the fast electron-hole separations in nPPy-TiO₂ nanocomposites.

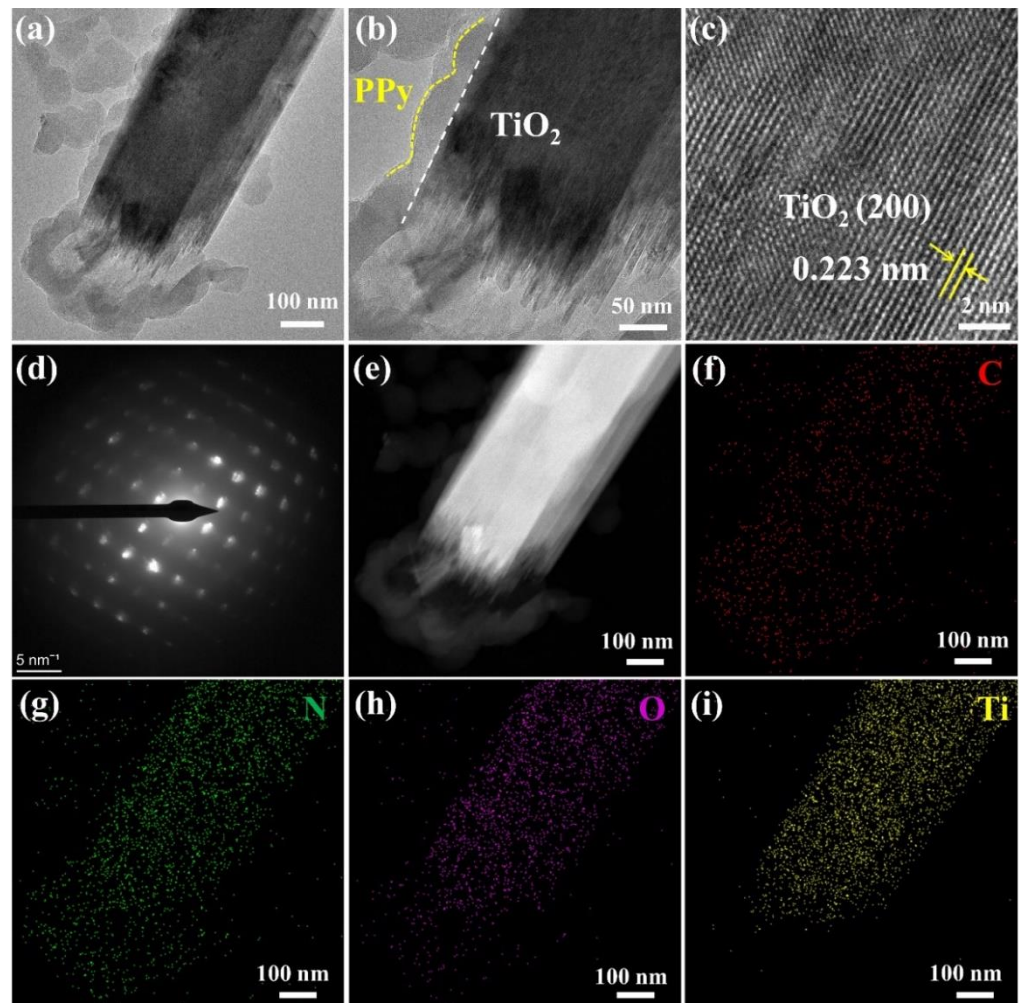


Figure 3. TEM images (a,b), HRTEM image (c), and the corresponding selected area electron diffraction pattern (d), STEM image (e), and the corresponding elemental mapping images (f–i) of 3PPy-TiO₂.

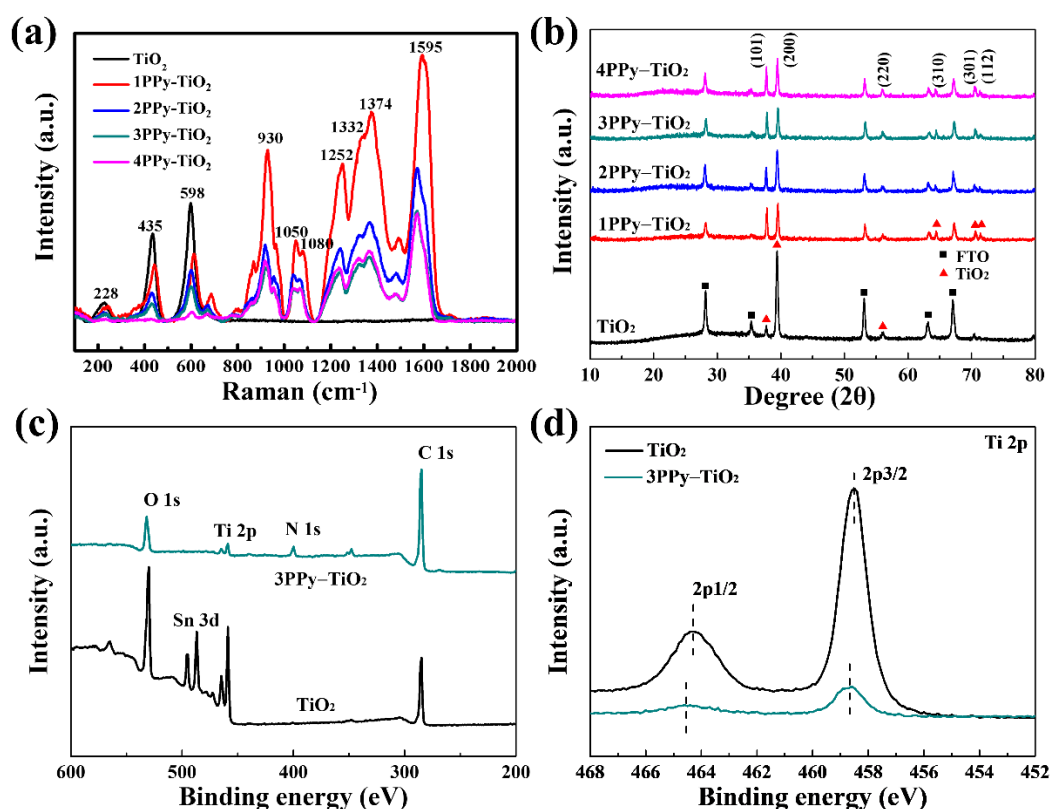


Figure 4. Raman spectra (a) and XRD patterns (b) of pure TiO_2 and nPPy- TiO_2 nanocomposites prepared by different deposition times; XPS surveys (c) and high-resolution Ti2p spectra (d) of pure TiO_2 and 3PPy- TiO_2 .

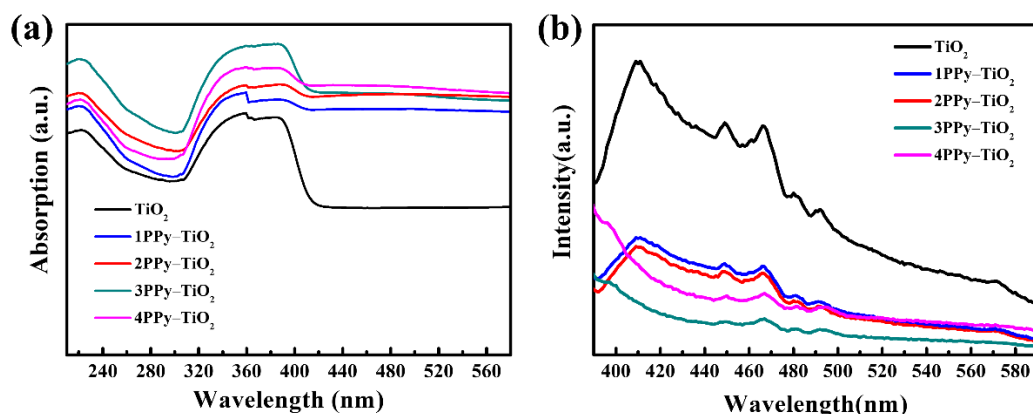


Figure 5. UV-Vis absorption spectra (a) and photoluminescence spectrum (b) of pure TiO_2 and nPPy- TiO_2 nanocomposites prepared by different deposition times.

3.2. UV Photo-Detection Properties of the FTO-nPPy- TiO_2 -FTO Devices

FTO- TiO_2 -FTO and FTO-nPPy- TiO_2 -FTO devices were fabricated to investigate the UV photo-detection properties. Figure 6 show the I-t curves detected with different UV light illuminations, where FTO-nPPy- TiO_2 -FTO devices presented enhanced photocurrent responses while the FTO- TiO_2 -FTO device showed almost no photocurrent, suggesting that the deposition of PPy film promoted the UV photo-detection property of TiO_2 . The photocurrent would immediately increase when FTO-nPPy- TiO_2 -FTO devices were irradiated with UV light. In particular, the FTO-3PPy- TiO_2 -FTO device exhibited the strongest photocurrent due to the proper thickness of PPy film. The FTO-3PPy- TiO_2 -FTO device had a maximum photocurrent of 6.0×10^{-7} A at 254 nm irradiation and 2.5×10^{-6} A at 365 nm irradiation, which was superior to the maximum photocurrent of 2.7×10^{-7} A

at 254 nm irradiation and 1.4×10^{-6} A at 365 nm irradiation of the FTO-4PPy-TiO₂-FTO device, the maximum photocurrent of 1.0×10^{-7} A at 254 nm irradiation and 0.8×10^{-6} A at 365 nm irradiation of the FTO-1PPy-TiO₂-FTO device, and the maximum photocurrent of 2.0×10^{-7} A at 254 nm irradiation and 0.2×10^{-6} A at 365 nm irradiation of the FTO-2PPy-TiO₂-FTO device. The I-V curves measured at dark and different UV light illuminations of the FTO-3PPy-TiO₂-FTO device in Figure S2 showed a rectifier phenomenon induced by a p-n heterojunction. Furthermore, the FTO-3PPy-TiO₂-FTO device had the highest current under 365 nm wavelength UV light. In fact, under UV light, photoelectrons might be efficiently inserted in the TiO₂ conduction band and subsequently into PPy, which accelerated the separation of photogenerated charges and led to the high photocurrent of the FTO-3PPy-TiO₂-FTO device. By comparing Figure 6a,b, it was found that the photocurrent when UV light was irradiated at 365 nm was higher than that at 254 nm, indicating that the assembled device should hold great promise as a UV-detector at 365 nm. Accordingly, the FTO-3PPy-TiO₂-FTO device exhibited good performance with sensitivity of 41.7, responsivity of 3.5×10^{-3} A/W, and detectivity of 2.1×10^{12} Jones, which outperforms the TiO₂-based devices in previous literature as shown in Table S1.

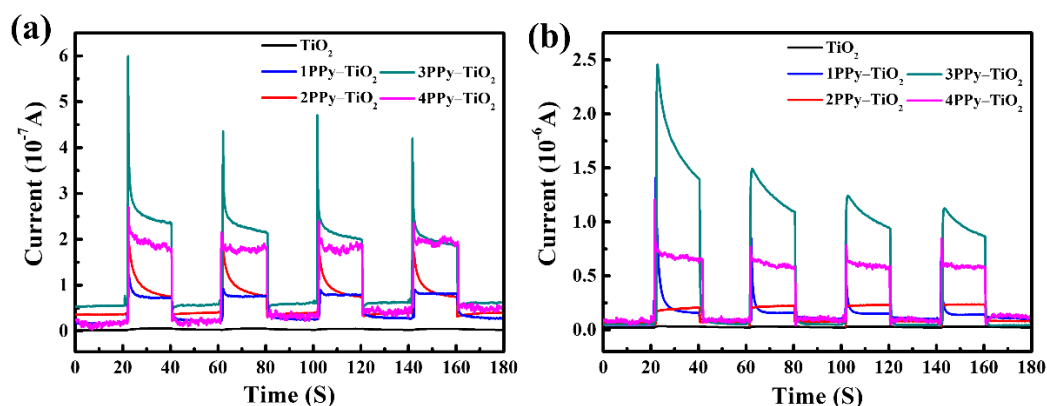


Figure 6. I-t curves of FTO-TiO₂-FTO and FTO-nPPy-TiO₂-FTO devices prepared by different deposition times with 254 nm ((a), 500 $\mu\text{W}/\text{cm}^2$) and 365 nm ((b), 470 $\mu\text{W}/\text{cm}^2$) UV light illumination.

Electrochemical impedance spectroscopy (EIS) was further carried out to study the interfacial charge transfer dynamics of the fabricated FTO-nPPy-TiO₂-FTO devices. As can be seen from the Nyquist plots in Figure 7, well-defined semi-circles that reflected the charge transfer resistance were observed. The diameters of the semi-circles were sorted as follows: 1PPy-TiO₂ > 2PPy-TiO₂ > 4PPy-TiO₂ > 3PPy-TiO₂, which was consistent with the order of photocurrent magnitude. Notably, the FTO-3PPy-TiO₂-FTO device had the smallest semi-circle among the four devices, denoting the lowest interfacial charge transfer resistance between PPy and TiO₂ [37]. This might stem from the strong interaction between PPy film and TiO₂ nanorod arrays, which greatly enhanced the optoelectronic properties of 3PPy-TiO₂. In addition, the results of this study show that there was a certain correlation between the interface conductivity and the thickness of the PPy layer in the PPy-TiO₂ semiconductor composite; too small or too large thickness was not conducive to the improvement of its conductivity. Furthermore, the sample of 3PPy-TiO₂ had the best electrical conductivity, which was also one of the important reasons for its best photoelectric response performance.

Based on the above results and discussion, the formation mechanism of photoelectric response and the built-in electric field of the p-n junction of PPy-TiO₂ are shown in Figure 8. The dominated holes were easily lost in the p-type semiconductor of PPy, so the Fermi level (E_F) was close to the valence band (E_V). Similarly, in the n-type semiconductor of TiO₂, electrons were dominant, and they were easily lost, so the Fermi level was close to the conduction band (E_C). PPy was in close contact with the TiO₂ interface, and a p-n junction was formed at the interface to form a built-in electric field, as shown in Figure 8c. The built-

in electric field at equilibrium caused the energy band to bend so that the Fermi levels of the two types of semiconductors were at the same level, and there was no net current flow in the semiconductors. Figure 8a,b show the schematic diagram of the photoelectric response. When UV light was irradiated on PPy-TiO₂, photogenerated electron-hole pairs were excited in TiO₂, electrons were excited from the valence band of TiO₂ to the conduction band, and the presence of a built-in electric field effectively separated photogenerated electron-hole pairs to form a net current so that inspection signals could be collected. It can be seen from the mechanism diagram that the photocurrent was closely related to the light response nature of the photosensitive material itself and the strength of the built-in electric field. Improving the photoresponse performance of the UV detector can be achieved by improving the photoresponse properties of the photosensitive material itself, such as surface doping modification. In addition, the performance of the UV photodetector can be improved by enhancing the strength of the built-in electric field at the interface of the composite. The results show that there was a certain relationship between the intensity of the electric field and the thickness of the semiconductor layer. That is, the thickness of the semiconductor layer had an optimal value. When the thickness of PPy is too small, the built-in electric field formed is weak, and when the thickness of PPy is too large, the conductivity may be weakened.

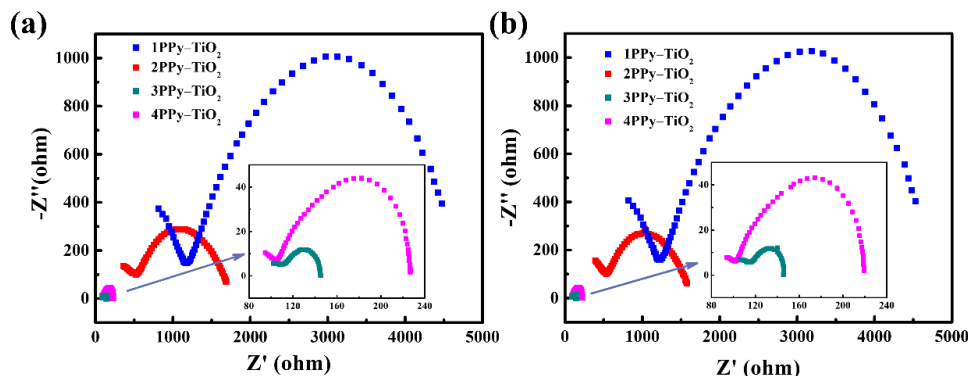


Figure 7. Nyquist plots of FTO-nPPy-TiO₂-FTO devices prepared by different deposition times with 254 nm (a) and 365 nm (b) UV light illumination.

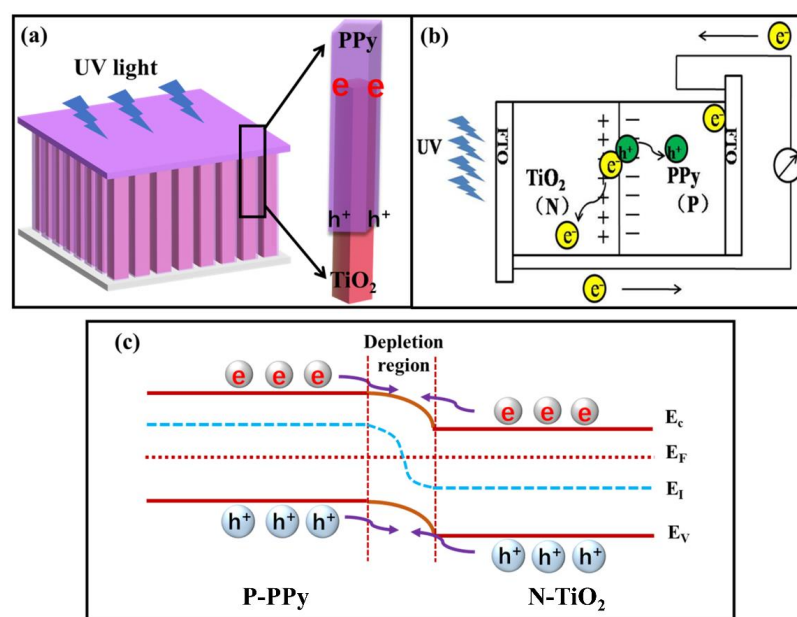


Figure 8. Schematic diagram of photoelectric response (a,b) and the formation mechanism of the built-in electric field of the p-n junction in PPy-TiO₂ composites (c).

4. Conclusions

In summary, the TiO₂ nanorod arrays were successfully prepared by a simple hydrothermal method. Additionally, a PPy film deposited-TiO₂ nanorod arrays was constructed by simple in situ oxidative polymerization, and the nanocomposites served as materials for UV photodetectors. The thickness of the PPy layer in PPy-TiO₂ composite material can be effectively regulated by the deposition times. Additionally, the thickness of the PPy layer can be effectively controlled around 20 nm~200 nm. Furthermore, there was a strong interaction between the TiO₂ nanorod arrays film and the PPy layer. Additionally, a p-n junction formed between PPy and TiO₂, which inhibited the recombination of photo-generated carriers in TiO₂, leading to better UV photo-detection performance of PPy-TiO₂ than pure TiO₂ nanorod arrays. The photodetectors fabricated with 3PPy-TiO₂ showed the best performance with a sensitivity of 41.7 and responsivity of 3.5×10^{-3} A/W, which was mainly due to their excellent electrical conductivity. This work provides a facile method to prepare TiO₂-based nanocomposites for UV photodetectors and is expected to be extended to other fields, including electrochemical storage and microwave-absorbing.

Supplementary Materials: The following supporting information can be downloaded at: <https://www.mdpi.com/article/10.3390/chemosensors10070277/s1>, Figure S1: TEM image (a) of TiO₂ and SEM image (b) of TiO₂-FTO film. Figure S2: The I-V curves of the FTO-3PPy-TiO₂-FTO device. Table S1: The comparison of results between previous reported PDs and our devices [20,38–41].

Author Contributions: Conceptualization, H.W. and P.Q.; formal analysis, H.W.; investigation, P.Q.; data curation, H.W. and P.Q.; writing—original draft preparation, H.W., H.-L.S. and H.-X.W.; writing—review and editing, B.-K.L. and Y.-B.X.; visualization, H.-L.S.; supervision, Y.-H.F. and W.W.; project administration, Y.-H.F. and W.W.; funding acquisition, H.W., Y.-H.F. and W.W. All authors have read and agreed to the published version of the manuscript.

Funding: This research was funded by the National Natural Science Foundation of China (NSFC) (No. 21908071, 22174027, 52001080), the Natural Science Foundation of Guangdong (No. 2020A1515011319), the Research Fund Program of Guangdong Provincial Key Lab of Green Chemical Product Technology (No. GC202107), the Joint Research Institute Fund of Guangzhou University and Guangdong Institute of Corrosion Science and Technology Innovation (20210209), the Key Laboratory of Pulp and Paper Science and Technology of Ministry of Education of China (No. KF201902), Natural Science Foundation of Shandong Province (ZR2020QB197), CAS Key Laboratory of Renewable Energy (No. E129kf0301). We thank Long-Wen Chen for the original draft preparation.

Institutional Review Board Statement: Not applicable.

Informed Consent Statement: Not applicable.

Data Availability Statement: Not applicable.

Conflicts of Interest: The authors declare no conflict of interest.

References

1. Chen, J.; Ouyang, W.; Yang, W.; He, J.; Fang, X. Recent Progress of Heterojunction Ultraviolet Photodetectors: Materials, Integrations, and Applications. *Adv. Funct. Mater.* **2020**, *30*, 1909909. [[CrossRef](#)]
2. Ma, H.; Zhang, H.; Fang, J.; Liu, X.; Wang, S.; Xie, M. Fabrication of Au-Cu Ordered Metallic Nanoparticle Arrays and Their Optical Properties. *Chin. J. Rare Met.* **2020**, *44*, 916–926.
3. Li, S.; Deng, T.; Zhang, Y.; Li, Y.; Yin, W.; Chen, Q.; Liu, Z. Solar-blind ultraviolet detection based on TiO₂ nanoparticles decorated graphene field-effect transistors. *Nanophotonics* **2019**, *8*, 899–908. [[CrossRef](#)]
4. Yang, T.; Chen, S.; Li, X.; Xu, X.; Gao, F.; Wang, L.; Chen, J.; Yang, W.; Hou, X.; Fang, X. High-Performance SiC Nanobelt Photodetectors with Long-Term Stability against 300 °C up to 180 Days. *Adv. Funct. Mater.* **2019**, *29*, 1806250. [[CrossRef](#)]
5. Li, X.; Ma, H.; Wang, X.; Chen, F.; Zeng, X. Structural and Luminescent Properties of Eu, Mg Co-doped GaN. *Chin. J. Rare Met.* **2020**, *44*, 1170–1176.
6. Zheng, K.-G.; Yang, T.-Y.; Guo, Z. Porous Pb-Doped ZnO Nanobelts with Enriched Oxygen Vacancies: Preparation and Their Chemiresistive Sensing Performance. *Chemosensors* **2022**, *10*, 96. [[CrossRef](#)]
7. Nguyen, T.; Patel, M.; Kim, S.-H.; Mir, R.; Yi, J.-S.; Dao, V.-A.; Kim, J.-D. Transparent photovoltaic cells and self-powered photodetectors by TiO₂/NiO heterojunction. *J. Power Sources* **2021**, *481*, 228865. [[CrossRef](#)]

8. Wang, H.; Qin, P.; Yi, G.; Zu, X.; Zhang, L.; Hong, W.; Chen, X. A high-sensitive ultraviolet photodetector composed of double-layered TiO₂ nanostructure and Au nanoparticles film based on Schottky junction. *Mater. Chem. Phys.* **2017**, *194*, 42–48. [[CrossRef](#)]
9. Zheng, W.; Dong, Y.; Li, T.; Chen, J.; Chen, X.; Dai, Y.; He, G. MgO blocking layer induced highly UV responsive TiO₂ nanoparticles based self-powered photodetectors. *J. Alloys Compd.* **2021**, *869*, 159299. [[CrossRef](#)]
10. Tian, A.; Shi, X.; Tan, H.; Li, B.; Ma, J.; Yang, H. Preparation and Photocatalytic Properties of Ni Doped TiO₂ Nanotube. *Chin. J. Rare Met.* **2021**, *45*, 41–46.
11. Haidry, A.; Fatima, Q.; Mehmood, A.; Shahzad, A.; Ji, Y.; Saruhan, B. Adsorption Kinetics of NO₂ Gas on Pt/Cr-TiO₂/Pt-Based Sensors. *Chemosensors* **2022**, *10*, 11. [[CrossRef](#)]
12. Zhang, D.; Liu, C.; Yin, B.; Xu, R.; Zhou, J.; Zhang, X.; Ruan, S. Organics filled one-dimensional TiO₂ nanowires array ultraviolet detector with enhanced photo-conductivity and dark-resistivity. *Nanoscale* **2017**, *9*, 9095–9103. [[CrossRef](#)] [[PubMed](#)]
13. Zheng, X.; Sun, Y.; Qin, H.; Ji, Z.; Chi, H. Interface engineering on ZnO/Au based Schottky junction for enhanced photoresponse of UV detector with TiO₂ inserting layer. *J. Alloys Compd.* **2020**, *816*, 152537. [[CrossRef](#)]
14. Ouyang, W.; Teng, F.; Fang, X. High Performance BiOCl Nanosheets/TiO₂ Nanotube Heterojunction UV Photodetector: The Influences of Self-Induced Inner Electric Fields in the BiOCl Nanosheets. *Adv. Funct. Mater.* **2018**, *28*, 1707178. [[CrossRef](#)]
15. Yang, D.; Du, F.; Ren, Y.; Kang, T.; Hu, P.; Teng, F.; Fan, H. A high-performance NiO/TiO₂ UV photodetector: The influence of the NiO layer position. *J. Mater. Chem. C* **2021**, *9*, 14146–14153. [[CrossRef](#)]
16. Wang, Y.; Chen, L.; Zhou, H.; Wei, K.; Zhu, Z.; Xie, E.; Cao, W.; Han, W. Rutile TiO₂ nanowire arrays interconnected with ZnO nanosheets for high performance electrochemical UV sensors. *J. Mater. Chem. C* **2019**, *7*, 8011–8018. [[CrossRef](#)]
17. Mojtabavi, E.A.; Nasirian, S. Flexible self-powered ultraviolet-visible photodetector based on polyaniline-titanium dioxide heterostructures: The study of the rearrangement of layers. *Appl. Surf. Sci.* **2019**, *492*, 189–198. [[CrossRef](#)]
18. Mojtabavi, E.A.; Nasirian, S. A self-powered UV photodetector based on polyaniline/titania nanocomposite with long-term stability. *Opt. Mater.* **2019**, *94*, 28–34. [[CrossRef](#)]
19. Zhang, H.; Abdiryim, T.; Jamal, R.; Li, J.; Liu, H.; Kadir, A.; Zou, D.; Che, Y.; Serkjan, N. Self-powered TiO₂ NRs UV photodetectors: Heterojunction with PTh and enhanced responsivity by Au nanoparticles. *J. Alloys Compd.* **2022**, *899*, 163279. [[CrossRef](#)]
20. Che, Y.; Zhang, H.; Abdiryim, T.; Jamal, R.; Kadir, A.; Helil, Z.; Liu, H. Ultraviolet photodetectors based on TiO₂ nanorod arrays/PEDOT-type conducting polymers. *Opt. Mater.* **2021**, *122*, 111805. [[CrossRef](#)]
21. Kareem, O.A.; Mohameed, S.J.; Ibrahim, I.M. The importance of doping TiO₂ into polypyrrol nanofibers to improve their optical sensitivity. *J. Phys. Conf. Ser.* **2021**, *2114*, 012057. [[CrossRef](#)]
22. Qin, P.; Yi, G.; Zu, X.; Wang, H.; Tan, M.; Luo, H. Preparation of graphene-TiO₂ nanocomposite films and its photocatalytic performances on degradation of Rhodamine B. *Pigm. Resin Technol.* **2018**, *47*, 79–85. [[CrossRef](#)]
23. Li, S.; Yin, W.; Li, Y.; Sun, J.; Zhu, M.; Liu, Z.; Deng, T. High sensitivity ultraviolet detection based on three-dimensional graphene field effect transistors decorated with TiO₂ NPs. *Nanoscale* **2019**, *11*, 14912–14920. [[CrossRef](#)] [[PubMed](#)]
24. Gao, Y.; Xu, J.; Shi, S.; Dong, H.; Cheng, Y.; Wei, C.; Zhang, X.; Yin, S.; Li, L. TiO₂ Nanorod Arrays Based Self-Powered UV Photodetector: Heterojunction with NiO Nanoflakes and Enhanced UV Photoresponse. *ACS Appl. Mater. Interfaces* **2018**, *10*, 11269–11279. [[CrossRef](#)] [[PubMed](#)]
25. Liao, Z.; Ma, M.; Tong, Z.; Wang, R.; Bi, Y.; Chen, Y.; Chung, K.-L.; Ma, Y. Fabrication of ZnFe₂O₄/C@PPy composites with efficient electromagnetic wave absorption properties. *J. Colloid Interf. Sci.* **2021**, *602*, 602–611. [[CrossRef](#)] [[PubMed](#)]
26. Bi, Y.; Ma, M.; Liu, Y.; Tong, Z.; Wang, R.; Chung, K.-L.; Ma, A.; Wu, G.; Ma, Y.; He, C.; et al. Microwave absorption enhancement of 2-dimensional CoZn/C@ MoS₂@ PPy composites derived from metal-organic framework. *J. Colloid Interf. Sci.* **2021**, *600*, 209–218. [[CrossRef](#)]
27. He, N.; Yang, X.; Shi, L.; Yang, X.; Lu, Y.; Tong, G.; Wu, W. Chemical conversion of Cu₂O/PPy core-shell nanowires (CSNWs): A surface/interface adjustment method for high-quality Cu/Fe/C and Cu/Fe₃O₄/C CSNWs with superior microwave absorption capabilities. *Carbon* **2020**, *166*, 205–217. [[CrossRef](#)]
28. Zhao, D.; Dai, M.; Zhao, Y.; Liu, H.; Liu, Y.; Wu, X. Improving electrocatalytic activities of FeCo₂O₄@FeCo₂S₄@PPy electrodes by surface/interface regulation. *Nano Energy* **2020**, *72*, 104715. [[CrossRef](#)]
29. Bi, Y.; Ma, M.; Liao, Z.; Tong, Z.; Chen, Y.; Wang, R.; Ma, Y.; Wu, G. One-dimensional Ni@Co/C@PPy composites for superior electromagnetic wave absorption. *J. Colloid Interface Sci.* **2022**, *605*, 483–492. [[CrossRef](#)]
30. Ding, J.; Wang, L.; Zhao, Y.; Xing, L.; Yu, X.; Chen, G.; Zhang, J.; Che, R. Boosted interfacial polarization from multishell TiO₂@Fe₃O₄@PPy heterojunction for enhanced microwave absorption. *Small* **2019**, *15*, 1902885. [[CrossRef](#)]
31. Yan, S.; Li, Y.; Xie, F.; Wu, J.; Jia, X.; Yang, J.; Song, H.; Zhang, Z. Environmentally safe and porous MS@TiO₂@PPy monoliths with superior visible-light photocatalytic properties for rapid oil–water separation and water purification. *ACS Sustain. Chem. Eng.* **2020**, *8*, 5347–5359. [[CrossRef](#)]
32. Ha, J.-U.; Lee, J.; Abbas, M.-A.; Lee, M.-D.; Lee, J.; Bang, J.-H. Designing hierarchical assembly of carbon-coated TiO₂ nanocrystals and unraveling the role of TiO₂/carbon interface in lithium-ion storage in TiO₂. *ACS Appl. Mater. Interfaces* **2019**, *11*, 11391–11402. [[CrossRef](#)] [[PubMed](#)]
33. Li, Z.-L.; Li, Z.-Q.; Zuo, C.; Fang, X. Application of Nanostructured TiO₂ in UV Photodetectors: A Review. *Adv. Mater.* **2022**, 2109083. [[CrossRef](#)] [[PubMed](#)]

34. Tang, H.; Berger, H.; Schmid, P.; Lévy, F.; Burri, G. Photoluminescence in TiO₂ anatase single crystals. *Solid State Commun.* **1993**, *87*, 847–850. [[CrossRef](#)]
35. Maurya, A.; Chauhan, P.; Mishra, S.K.; Srivastava, R.K. Structural, optical and charge transport study of rutile TiO₂ nanocrystals at two calcination temperatures. *J. Alloys Compd.* **2011**, *509*, 8433–8440. [[CrossRef](#)]
36. Serpone, N.; Lawless, D.; Khairutdinov, R. Size effects on the photophysical properties of colloidal anatase TiO₂ particles: Size quantization versus direct transitions in this indirect semiconductor? *J. Phys. Chem.* **1995**, *99*, 16646–16654. [[CrossRef](#)]
37. Hsu, C.-P.; Lee, K.-M.; Huang, J.T.-W.; Lin, C.-Y.; Lee, C.-H.; Wang, L.-P.; Tsai, S.-Y.; Ho, K.-C. EIS analysis on low temperature fabrication of TiO₂ porous films for dye-sensitized solar cells. *Electrochim. Acta* **2008**, *53*, 7514–7522. [[CrossRef](#)]
38. Zheng, L.; Yu, P.; Hu, K.; Teng, F.; Chen, H.; Fang, X. Scalable-production, self-powered TiO₂ nanowell–organic hybrid UV photodetectors with tunable performances. *ACS Appl. Mater. Interfaces* **2016**, *8*, 33924–33932. [[CrossRef](#)]
39. Zheng, L.; Deng, X.; Wang, Y.; Chen, J.; Fang, X.; Wang, L.; Shi, X.; Zheng, H. Self-powered flexible TiO₂ fibrous photodetectors: Heterojunction with P3HT and boosted responsivity and selectivity by Au nanoparticles. *Adv. Funct. Mater.* **2020**, *30*, 2001604. [[CrossRef](#)]
40. Chen, D.; Wei, L.; Meng, L.; Wang, D.; Chen, Y.; Tian, Y.; Yan, S.; Mei, L.; Jiao, J. High-performance self-powered UV detector based on SnO₂-TiO₂ nanomace arrays. *Nanoscale Res. Lett.* **2018**, *13*, 92. [[CrossRef](#)]
41. Zhou, M.; Wu, B.; Zhang, X.; Cao, S.; Ma, P.; Wang, K.; Fan, Z.; Su, M. Preparation and UV photoelectric properties of aligned ZnO–TiO₂ and TiO₂–ZnO core–shell structured heterojunction nanotubes. *ACS Appl. Mater. Interfaces* **2020**, *12*, 38490–38498. [[CrossRef](#)] [[PubMed](#)]